PAPER

Check for updates

Electrocatalytic valorization of 5-hydroxymethylfurfural coupled with hydrogen production using tetraruthenium-containing polyoxometalate-based composites†

Hui Zhou,[a] Yuanyuan Dong, [ID] *[a] Xing Xin,[a] Manzhou Chi,[a] Tinglu Song[b] and Hongjin Lv [ID] *[a]

Electrocatalytic biomass valorization represents a promising route to produce sustainable and carbon-neutral products, especially when coupled with hydrogen production. Here we report a **Ru₄**/PEI-rGO electrocatalyst, prepared by electrostatic integration of a tetraruthenium-containing polyoxometalate, $Rb_8K_2[Ru_4(\mu\text{-}O)_4(\mu\text{-}OH)_2(H_2O)_4(\gamma\text{-}SiW_{10}O_{36})_2]\cdot25H_2O$ (**Ru₄**), with polyethyleneimine (PEI) modified rGO, which can efficiently electrocatalyze biomass-derived 5-hydroxymethylfurfural (HMF) to value-added furanic products simultaneously coupled with H_2 production in near neutral media. Under minimally optimized conditions, the conversion of HMF and the yield of H_2 reached 50.8% and 55.4 µmol after 6 hour electrocatalysis at 0.94 V *vs.* Ag/AgCl, respectively. 2,5-Diformylfuran (DFF) was detected as the dominant oxidation product with a selectivity of 66.2%. The faradaic efficiencies (FEs) of the anode and cathode reached 97.0 ± 3% and 100.2 ± 2%, respectively. In the presence of the 2,2,6,6-tetramethylpiperidinyloxyl (TEMPO) additive, the conversion of HMF reached 99.7%, and the distribution of the oxidation product has been greatly altered, wherein furanic carboxyl products are dominant. Various electrochemical characterization studies and spectrogram analyses, especially Fourier Transformed Alternating Current (FTAC) voltammetry, were employed to disclose that Ru^V centers were catalytically active species, and the three-electron oxidized **Ru₄** species are responsible for the excellent electrocatalytic activity. Long-term electrocatalysis demonstrated that the present **Ru₄**/PEI-rGO composite possessed good stability for catalysis.

Yuanyuan Dong received her PhD degree from Tianjin University under the supervision of Prof. Xinbin Ma. After finishing the postdoctoral training with Prof. Shijun Liao at South China University of Technology and Prof. Qi Chen at Beijing Institute of Technology (BIT), she joined the School of Chemistry and Chemical Engineering at BIT as an Assistant Professor. Her current research is focused on the material design of polyoxometalate-semiconductor composites, electro-/photocatalysis for renewable energy conversion, and value-added transformation of organic chemicals.

Introduction

With the increasing global demand for environmental protection and energy requirements, the development of renewable energy, such as the electrocatalytic conversion of biomass, has inspired great research interest.[1–5] HMF, as a top-rated biomass-derived building block chemical, can be used as a versatile precursor for the production of fine chemicals, plastics, pharmaceuticals, and liquid fuels.[6] HMF can be oxidized to a wide range of chemicals including DFF, 5-hydroxymethyl-2-furancarboxylic acid (HMFCA), 5-formyl-2-furancarboxylic acid (FFCA) and 2,5-furandicarboxylic acid (FDCA).[7] During the past few years, a large number of electrocatalytic/photo electrocatalytic systems have been reported, including noble metal catalysts (Pt,[8] Au/Pd,[9] and Ru pincer[10]), non-noble metal catalysts ($NiO/Ni(OH)_2$,[11] Ni NPs,[12] Ni_2P,[6] Ni_xB,[13] $NiCo_2O_4$,[14] $CuNi(OH)_2/C$,[15] and $BiVO_4$,[16]) and metal-free catalysts (B/N–C[17]).

aMOE Key Laboratory of Cluster Science, Beijing Key Laboratory of Photoelectroic/Electrophotonic Conversion, School of Chemistry and Chemical Engineering, Beijing Institute of Technology, Beijing 102488, P. R. China. E-mail: dyy1111@bit.edu.cn; hlv@bit.edu.cn

bExperimental Center of Advanced Materials, School of Materials Science & Engineering, Beijing Institute of Technology, China

† Electronic supplementary information (ESI) available. See https://doi.org/10.1039/d2ta02148j

This journal is © The Royal Society of Chemistry 2022

*J. Mater. Chem. A*, 2022, **10**, 19963–19971 | **19963**

These catalysts were reported to effectively catalyze the oxidation of HMF to FDCA in strong alkali electrolyte *via* path II (Scheme 1). Interestingly, DFF is also a high value-added platform chemical and can be used either as a monomer, or as starting material in the synthesis of furan-urea resins, foams, binders, and pharmaceuticals.[18] However, only a few reports about the oxidation of HMF *via* path I exist (Scheme 1).[19] Additionally, it is also an interesting topic to regulate the product distribution (furanic aldehyde and furanic carboxyl) during the valorization of HMF, whereas there are rarely related reports so far according to our knowledge. Therefore, it is highly desirable to develop efficient electrocatalysts for the electro-oxidation of HMF with adjustable value-added products.

Polyoxometalates (POMs), a large class of early transition-metal (*e.g.* V^V, Nb^V, Ta^V, Mo^{VI}, and W^{VI}) oxygen-anion clusters with usually d^0 electronic configuration,[20] have been considered as one of the promising multi-electron transfer catalysts due to their rich redox chemistry, compositional tunability, and excellent electron reservoir capacity. POMs have been widely applied in photo/electrocatalysis fields including the HER,[21–24] OER,[25–27] and CO$_2$RR.[28–30] Additionally, POMs ((KCl$_4$)Na$_7$[(β-CD)$_3$(SiW$_{12}$O$_{40}$)]·9H$_2$O,[31] (THA)$_3$[SbW$_9$O$_{33}$(RSiO)$_3$Ti(OiPr)],[32] (Gd$_4$(H$_2$O)$_{26}$[WZn{Cu(H$_2$O)}$_2$(ZnW$_9$O$_{34}$)$_2$]·24H$_2$O,[33] [Co(BBPTZ)$_3$][HPMo$_{12}$O$_{40}$]·24 H$_2$O,[34] [TMGHA]$_{2.4}$H$_{0.6}$PW$_{12}$O$_{40}$,[35] and H$_x$PMo$_{12}$O$_{40}$⊂H$_4$Mo$_{72}$Fe$_{30}$(CH$_3$COO)$_{15}$O$_{254}$ [36] were also reported to effectively oxidize alcohols, alkenes, and thiophene with H$_2$O$_2$ or O$_2$ as an oxidant at appropriate temperatures. However, there are few reports on the electrocatalytic oxidation of biomass derivatives using POMs as electrocatalysts, especially while integrating with hydrogen production to construct a more valuable electrochemical coupling system.[37] Moreover, POMs, with a specific elemental composition and distinct geometric structure, could be easily used as a model catalyst to investigate catalytically active sites and the reaction mechanism. Therefore, it is an interesting topic to develop POM-based composite electrocatalysts to convert biomass into high value-added products and simultaneously produce hydrogen.

Herein, we report the preparation of a **Ru$_4$**/PEI-rGO composite *via* the electrostatic interaction of **Ru$_4$** POM and PEI modified rGO (Scheme 2a), which could efficiently electrocatalyze oxidation of HMF to value-added furanic products simultaneously coupled with hydrogen generation (Scheme 2b). The reaction parameters during the preparation of catalysts and the electrocatalytic process were further optimized, including the amount of PEI, the content of **Ru$_4$** POM, the loading quantity of the composite electrocatalyst onto carbon cloth, and the reaction atmosphere. The positive influences on electrocatalytic activities of the additive TEMPO were also investigated.
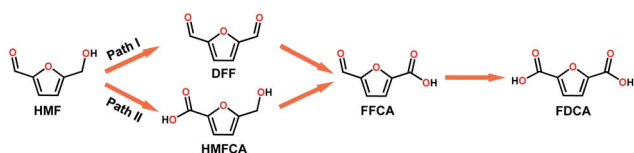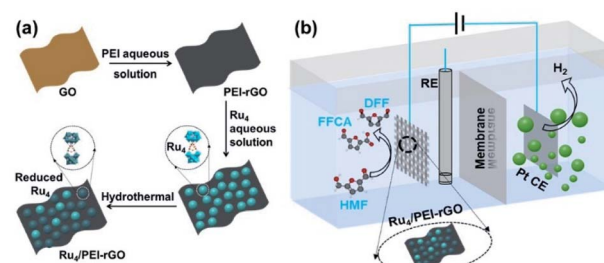
Scheme 2 The schematic diagrams of (a) the preparation route of Ru$_4$/PEI-rGO and (b) the electrocatalytic conversion of HMF coupled with hydrogen production system.

Various electrochemical characterization studies and spectrogram analyses, especially FTAC voltammetry, were employed to disclose the catalytically active species and further get insight into the electrocatalytic oxidation mechanism of HMF.

Results and discussion

The preparation of **Ru$_4$**/PEI-rGO is described in detail in the Experimental section. The hydrothermal temperature was determined based on the results of thermogravimetric (TG) and differential thermal analysis (DTA) (Fig. 1a). A weight loss of 5.87% is associated with the loss of 22 water molecules terminally bound to the Ru^{IV} centers as well as the accompanied endothermic process. The **Ru$_4$**-containing residue after TG analysis could be re-dissolved in water as a homogeneous and transparent solution (Fig. S1†), indicating that the molecular structure of **Ru$_4$** POM could be kept intact below 400 °C. Scheme 2a depicts the schematic synthetic diagram of **Ru$_4$**/PEI-rGO *via* electrostatic self-assembly, as revealed by the changes in zeta potential (ζ) (Fig. 1b).

Fig. 2 shows the Fourier transform infrared (FT-IR) spectra of GO, PEI-rGO, **Ru$_4$**/PEI-rGO, and **Ru$_4$** samples. The characteristic bands at 1052, 1225 cm^{-1}, 1401 and 1720 cm^{-1} marked with light yellow block were attributed to the vibration bands of C–O–C, O–H and C=O for GO, respectively.[38,39] After grafting with PEI molecules, the bands at 1052 and 1720 cm^{-1} completely disappear, along with obvious weakening of two peaks at 1401 (v_{O-H}) and 1225 (v_{C-O}) cm^{-1}. The strong band at 1618 cm^{-1} in GO is replaced by a band at 1640 cm^{-1} (light blue block) in PEI-rGO, which is attributed to the formation of amide bonds
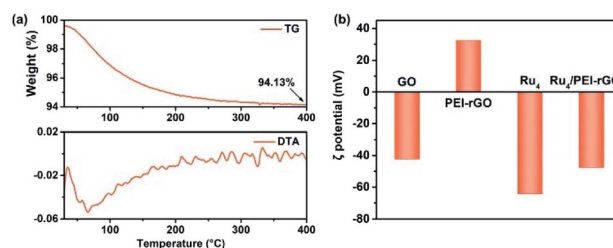

Fig. 1 (a) TG analysis (top) and DTA data (bottom) of the Ru$_4$/PEI-rGO sample. (b) Zeta potentials of GO, PEI-rGO, Ru$_4$, and Ru$_4$/PEI-rGO samples.
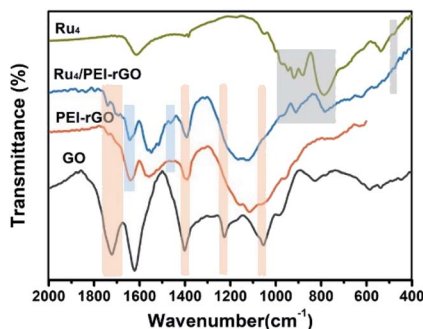

Scheme 1 Two possible pathways of HMF oxidation to their corresponding aldehydes and acids.

19964 | *J. Mater. Chem. A*, 2022, **10**, 19963–19971

This journal is © The Royal Society of Chemistry 2022

Fig. 2 FT-IR spectra of GO, PEI-rGO, Ru₄, and Ru₄/PEI-rGO samples.

because of the reduction of GO by PEI molecules. In addition, a new band at 1460 cm^{-1} (light blue block) appears in PEI-rGO which is assigned to the C–N stretching vibration.[40] These observations fully indicate the successful grafting of PEI molecules onto the GO surface, confirmed by the changes in ζ from −42.28 mV of GO to 32.35 mV of PEI-rGO (Fig. 1b). Additionally, the characterization bands marked with grey block identify the typical features of γ-disubstituted polytungstates (940 cm^{-1} W=O$_d$ stretching; 850 cm^{-1} W–O$_b$–W stretching of corner-sharing octahedron; 805–730 cm^{-1} W–O$_c$–W stretching of corner-sharing octahedron)[41] and a characteristic Ru–O–Ru mode (487 cm^{-1}),[42] showing the successful immobilization of Ru₄ onto the PEI-rGO surface, which is consistent with the changes in ζ from the 32.35 mV of PEI-rGO to −47.54 mV of Ru₄/PEI-rGO (Fig. 1b).

Ru₄/PEI-rGO displayed a transparent nanosheet morphology as illustrated by the transmission electron microscopy (TEM) images (Fig. 3 and S2†). Energy-dispersive X-ray (EDX) elemental analysis confirmed the presence of Ru, W, Si, and Rb elements (Fig. S3†). Moreover, the fine Ru₄ POM clusters were uniformly distributed on the PEI-rGO surface as evidenced by high-resolution TEM (left bottom image in Fig. 3) and high-angle annular dark-field scanning transmission electron microscopy (HAADF-STEM) and element mapping analysis (Fig. 3).
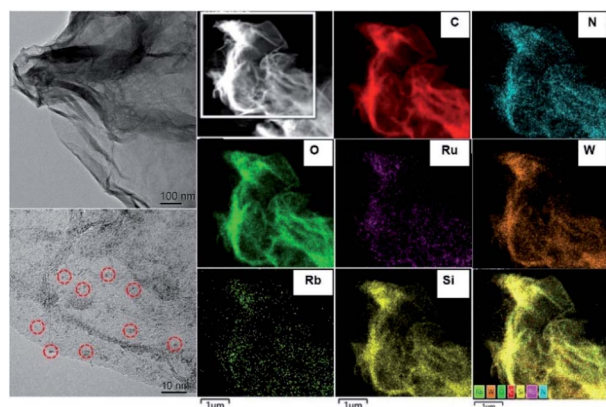
To further confirm the elemental composition and chemical oxidation state, XPS measurements were conducted on Ru₄ POM and the Ru₄/PEI-rGO composite. The W 4f, Ru 3p, Si 2p, and O 1s signals were clearly detected in the XPS survey spectra (Fig. S4†). The peaks at binding energies of 462.5 eV (Ru 3p$_{3/2}$) and 484.5 eV (Ru 3p$_{1/2}$) were attributed to the Ru^{IV} species (Fig. 4a). The peaks at 35.0 eV (W 4f$_{7/2}$) and 37.1 eV (W 4f$_{5/2}$) were assigned to the W^{VI} species (Fig. 4b), which is consistent with the literature report.[41] After immobilization, both the Ru 3p and W 4f XPS signals shifted negatively to lower binding energies, indicating the partially reduction of Ru₄ POM caused by the electron density shift from PEI-rGO to Ru₄ POM.

The electrocatalytic activity of the Ru₄/PEI-rGO composite was first evaluated by cyclic voltammetry (CV) and linear sweep voltammetry (LSV) analyses (Fig. 5a and b) in pH 6 HAc/NaAc buffer solution (0.5 M). Compared with rGO and PEI-rGO, the Ru₄/PEI-rGO composite exhibited obvious oxidation current at a relatively more negative onset potential. Additionally, the open-circuit potential also shifted to a more negative value (0.26 V vs. Ag/AgCl, Fig. 5a), indicating that Ru₄ POM has been reduced spontaneously by the HMF substrate. These observations imply that the Ru₄/PEI-rGO composite shows efficient electrocatalytic activity towards HMF oxidation. Upon electrocatalysis for 6 hour at 0.94 V vs. Ag/AgCl (Fig. 5c), the anode oxidation products were detected and quantified by high performance liquid chromatography (HPLC) (Fig. S5†), achieving 50.8% conversion of the HMF substrate with a total selectivity of anodic furanic products of 95.5%. Additionally, DFF dominated the anodic oxidation products with a selectivity of 66.2% (Fig. 5d). For rGO and PEI-rGO as control electrocatalysts, the yield of DFF is very low in spite of their high HMF conversion, which could be ascribed to the deep mineralization of HMF as illustrated by the extremely lower carbon balance (X_c) and the GC spectra of the gaseous products at the anode chambers (Fig. S6†). In terms of the cathodic product, a H₂ yield of 55.4 μmol was obtained in the Ru₄/PEI-rGO-electrocatalytic system. Additionally, faradaic efficiencies of the anode and cathode were basically consistent, indicating that the oxidation of HMF over Ru₄/PEI-rGO has effectively proceeded via the electrocatalytic process (Fig. 5e). Additionally, electrochemical impedance spectroscopy (EIS) measurements were performed at 0.94 V vs. Ag/AgCl for further investigating the electrochemical kinetics of HMF oxidation. As shown in Fig. 5f, the similar resistance indicated that the modification of PEI did not

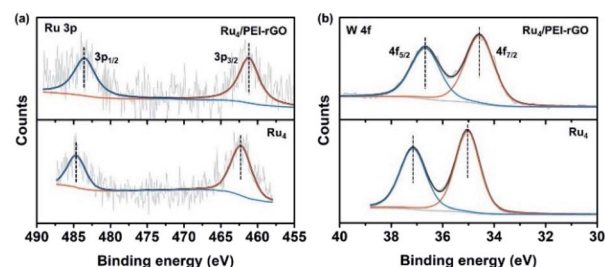Fig. 3 TEM and HAADF-STEM images and element mapping for the Ru₄/PEI-rGO electrocatalyst.

Fig. 4 The high-resolution (a) Ru 3p and (b) W 4f XPS spectra of Ru₄ and Ru₄/PEI-rGO.

This journal is © The Royal Society of Chemistry 2022

J. Mater. Chem. A, 2022, 10, 19963–19971 | 19965
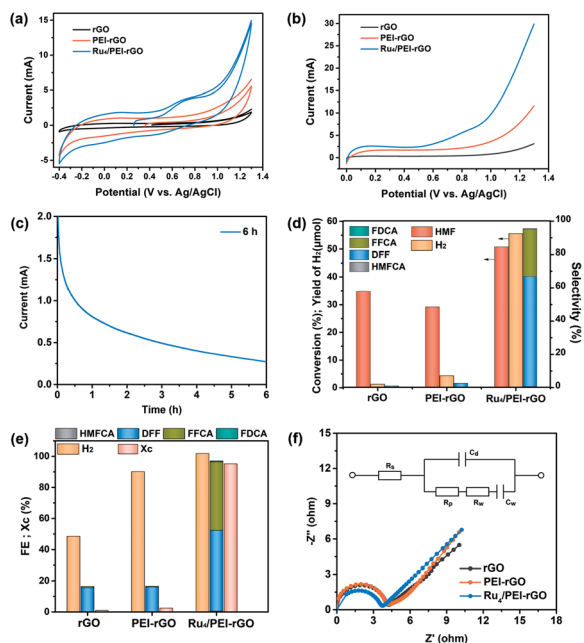
Fig. 5 (a) CV and (b) LSV curves of rGO, PEI-rGO and Ru$_4$/PEI-rGO electrocatalysts. (c) The $i-t$ response curve of Ru$_4$/PEI-rGO at 0.94 V vs. Ag/AgCl for 6 h. The conversion of HMF, the selectivity of liquid products and the yield of H$_2$ (d) and FE (e) of products for rGO, PEI-rGO and Ru$_4$/PEI-rGO electrocatalysts upon bulk electrolysis at 0.94 V vs. Ag/AgCl for 6 h at room temperature. (f) Nyquist plots for rGO, PEI-rGO and Ru$_4$/PEI-rGO in 5 mM HMF (0.5 M pH = 6 HAc/NaAc) at 0.94 V vs. Ag/AgCl and the equivalent circuit diagram.
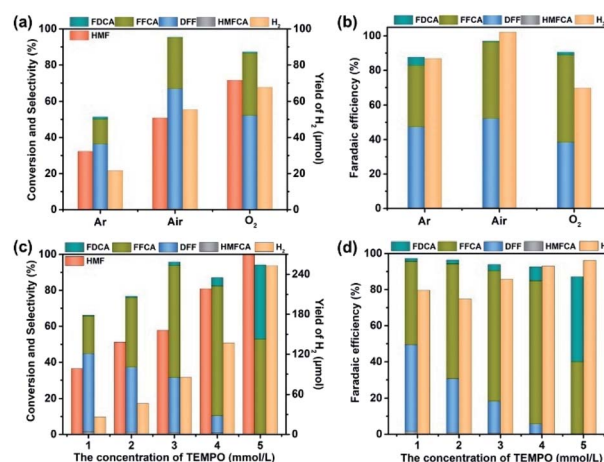

Fig. 6 The effects of the reaction atmosphere (a and b) and concentration of TEMPO (c and d) on the electrocatalytic activities of Ru$_4$/PEI-rGO.

influence the electron transfer between HMF and rGO during the electrocatalysis. Moreover, the smaller resistance implied a fast electron transfer between Ru$_4$ and HMF, and therefore Ru$_4$/PEI-rGO exhibited efficient electrocatalytic activity towards HMF oxidation.

We further optimized the reaction parameters during the preparation of catalysts and the electrocatalytic process, including the amount of PEI, the content of Ru$_4$ POM, the loading quantity of the composite electrocatalyst onto carbon cloth, the reaction atmosphere (Tables S1 and S2† and Fig. 6 and S7†), etc. Despite the higher conversion of HMF in an O$_2$ atmosphere, the faradaic efficiencies and the selectivity of oxidation products are inferior to those in an air atmosphere (Fig. 6a and b). Therefore, the subsequent electrocatalysis tests were all conducted in an air atmosphere using the above-mentioned optimized parameters. Additionally, the amount of Ru was determined to be 2.4 wt% for the optimized Ru$_4$/PEI-rGO electrocatalyst by inductively coupled plasma (ICP), which is highly cost-effective compared to the noble metal alloy-based electrocatalysts reported in the literature with similar electro-catalytic activities.[19] Compared with the reported noble metal-based electrocatalysts, Ru$_4$/PEI-rGO used in this work exhibited significant advantages in the electrooxidation of HMF to DFF at near-neutral electrolyte (Table S3†).

Careful inspection of the CV and LSV curves of the Ru$_4$/PEI-rGO-based electrode reveals an obvious oxidation peak at 0.7 V, identifying the indirect oxidation of HMF. It can be proposed

that Ru$_4$ is first electrooxidized to its active oxidizing state that could further oxidize HMF during the electrocatalytic process. The redox chemistry and multi-electron transfer capacity of POMs largely depend on the pH, applied voltage, and the electrolyte solution;[43] we thus investigated the influences of these parameters on the electrocatalytic activity. As shown in Table 1 (entries 1–3), the conversion of HMF gradually increased with increasing pH value, and DFF is still the dominant anodic oxidation product, whereas the selectivity of FFCA was gradually enhanced which could be attributed to the favorable formation of carboxyl products under alkaline conditions.[44] Given the higher furanic yield and faradaic efficiencies, the HAc/NaAc buffer solution (0.5 M) at pH 6 was selected as the optimized electrolyte. Then, the electrolysis has further been conducted at different applied voltages (Table 1, entries 2, 4, and 5). As shown by the experimental results, the yields of furanic products and H$_2$ gradually increased with the increment of applied voltages, which is more obvious in the lower voltage range. To avoid the oxygen evolution competing reaction, an applied voltage of 0.94 V was used for HMF electrooxidation.

Moreover, a commonly-used additive, TEMPO that was reported to effectively facilitate the selective transformation of primary alcohols into aldehydes by a 2e-transfer mechanism,[45] was further utilized to promote the electrocatalysis. As shown by entry 6 of Table 1, the conversion of HMF reached almost 100%, and the yield of H$_2$ was enhanced by 4.6 times with the addition of 1 eq. (5 mM) TEMPO, respectively. The furanic carboxyl products (FFCA and FDCA) dominated the oxidation products. The influence of the amount of TEMPO on the electrocatalytic activity was further investigated (Fig. 6c and d). Both the conversion of HMF and the yield of furanic products are proportionally increased with the increment of TEMPO. Moreover, the distribution of oxidation products changed significantly, and the carboxyl products won by a landslide. According to the enhanced electrocatalytic performance and the varied product distribution, it could be suspected that TEMPO can effectively

Table 1 Screening of reaction conditions for the electrocatalytic oxidation of HMF by Ru_4/PEI-rGO[a]tbl1fna

Entry	Conditions	HMF Con. (%)	HMFCA Sel. (%)	HMFCA FE (%)	DFF Sel. (%)	DFF FE (%)	FFCA Sel. (%)	FFCA FE (%)	FDCA Sel. (%)	FDCA FE (%)	Furanic Sel. (%)	FE of anode (%)	H$_2$ Yield (μmol)	H$_2$ FE (%)
1	pH 4, 0.94 V	33.5	0	0	41.0	67.5	6.7	21.9	0	0	47.6	89.4	11.3	86.4
2	pH 6, 0.94 V	50.8	0.7	0.6	66.2	51.7	28.3	44.2	0.3	0.6	95.5	97.1	55.4	100.2
3	pH 8, 0.94 V	56.9	1.0	0.8	52.5	43.4	30.5	50.5	0.3	0.7	84.3	95.4	46.0	92.4
4	pH 6, 0.8 V	47.1	0.6	0.6	39.0	45.6	22.9	52.3	0.8	3.6	63.3	100.2	33.5	85.2
5	pH 6, 0.6 V	30.7	0	0	24.2	77.9	4.6	29.7	0	0	28.8	100.6	6.5	100.3
6	+1 eq. TEMPO	99.7	0.17	0.07	0	0	52.6	40	41.4	47	94.2	87.1	253.0	96.2

[a] Conditions: 0.5 M HAc/NaAc buffer solution, HMF (5 mM), Ru_4/PEI-rGO catalysts (0.5 mg), bulk electrocatalysis for 6 h at applied voltage *vs.* Ag/AgCl.

promote the conversion of HMF to DFF, which is further oxidized to carboxyl products by Ru_4/PEI-rGO.

The above experimental observations further encouraged us to understand the redox behavior of the Ru_4/PEI-rGO composite in order to better illustrate the catalytically active species and the electrooxidation mechanism of HMF. Considering that direct current cyclic voltammetry cannot unambiguously distinguish the redox peaks of the potential active species from that of resting Ru^{IV} centers (Fig. 5a), FTAC voltammetry is therefore employed to better identify the redox behavior of Ru^{IV} centers by taking advantage of the fact that the higher harmonic components are sensitive to the fast-heterogeneous electron transfer process, but insensitive to the catalytic process.[46] Fig. 7a depicts the 1st–5th harmonic components of a FTAC voltammogram of Ru_4/PEI-rGO supported with a 1 cm^2 carbon cloth in pH 6 buffer solution containing 5 mM HMF. The shape of the 1st harmonic current is obviously different from that of the LSV curve, where the oxidation current of Ru^{IV} quickly reaches the limited value and further decreased (theoretically s-shaped curve).[47] Since the Ru^{IV} center is first oxidized to the oxidation state at lower voltage, the concomitant oxidation current reaches a maximum value as the voltage increases; meanwhile, the HMF oxidation process occurs, leading to a decline in the oxidation current of the Ru^{IV} center at increasing voltage. The reversible potentials of the $Ru^{IV/V}$ center were determined according to the criterion reported in the literature.[47] The potential was taken as the average of the valley potentials from forward and reverse scans of potential in the case of even harmonic components, while the average of the

peak potentials from both forward and reverse scans in the case of odd harmonic components was taken. Four well-defined one-electron transfer processes are shown in Fig. 7a assigned to the process **1**(0)/**1**(1), **1**(1)/**1**(2), **1**(2)/**1**(3), and **1**(3)/**1**(4) at reversible potentials of 0.58 V, 0.75 V, 0.94 V and 1.12 V, where **1** represents the Ru^{IV} core, and **1**(0) and **1**(x) stand for its initial form with the oxidation state Ru^{IV} and the x-electron oxidized form, respectively. The observed redox behavior is consistent with the results of Ru_4 POM in the homogeneous solution (Fig. S8†). The harmonic components of the FTAC voltammograms in pH 4 and pH 8 electrolyte solutions are shown in Fig. 7b and c, respectively. In the case of pH 4, the $Ru^{IV/V}$ redox processes are composed of two 1e-transfer processes (**1**(0)/**1**(1) and **1**(1)/**1**(2)) and one 2e-transfer process (**1**(2)/**1**(4)). In the case of pH 8, the $Ru^{IV/V}$ redox processes are composed of **1**(0)/**1**(1), **1**(1)/**1**(3), and **1**(3)/**1**(4) components. These observations were in good agreement with the results obtained in the homogeneous solution (Fig. S9 and S10†). Such pH-dependent redox behavior of $Ru^{IV/V}$ was also observed in the literature.[47]

At an applied voltage of 0.94 V during the electrolysis process, Ru_4 stayed at the oxidation state of **1**(3) in pH 6 and pH 8 electrolyte solutions but at an oxidation state of **1**(2) in pH 4 electrolyte solution (Fig. 7).The yield of furanic products at pH 6 reaches 48.5%, which is 3 times higher than that of the catalytic system (15.9%) at pH 4 (entries 1–3, Table 1). Therefore, it could be concluded that the discrepancy in oxidation states of Ru_4 resulted in the different electrocatalytic oxidation performances under three electrolyte conditions, wherein Ru_4/PEI-rGO in the oxidation state **1**(3) performed the best. Similar results have also been obtained by the electrolysis experiments of Ru_4/PEI-rGO at 0.6 V, 0.8 V, and 0.94 V, corresponding to the **1**(1), **1**(2), and **1**(3) oxidation states, respectively. Specifically, a furanic yield of 48.5% achieved at an applied potential of 0.94 V (entry 2, Table 1) was 5.5 times higher than that of the experiment at 0.6 V (8.8%, entry 5, Table 1), substantiating that the electrocatalytic activity largely depends on the proportion of the Ru^V species in the Ru_4/PEI-rGO composite.

To further understand the chemical environment and electronic properties of Ru_4/PEI-rGO, XPS measurements were carried out on Ru_4/PEI-rGO after 6 hour electrolysis at 0.94 V in pH 6 electrolyte solution. Compared with that of the fresh catalyst (Fig. S11a†), no obvious changes were observed for the
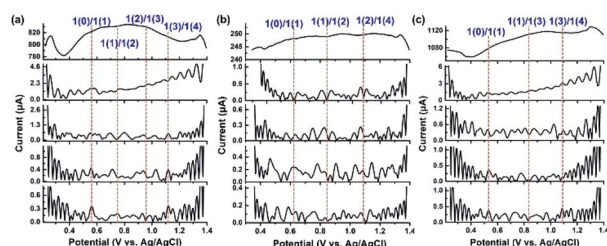

Fig. 7 1st to 5th (top to bottom) harmonic components of a FTAC voltammogram ($f = 10$ Hz, $\Delta E = 20$ mV, and scan rate = 92 mV s^{-1}) of Ru_4/PEI-rGO supported with a 1 cm^2 carbon cloth in (a) pH 6, (b) pH 4 and (c) pH 8 buffer solutions containing 5 mM HMF.

This journal is © The Royal Society of Chemistry 2022

J. Mater. Chem. A, 2022, **10**, 19963–19971 | **19967**

C 1s + Ru 3d XPS spectra (Fig. 8a), indicating good stability of the carbon substrate. The deconvoluted signal of Ru–OH (Fig. S11b†), assigned to the water molecules bounded to Ru^{IV} centers,[48] significantly decreased after electrolysis (Fig. 8b), proving the active participation of Ru^{IV} centers during electrocatalysis. As illustrated by CV and FTAC voltammogram analyses, the initial Ru^{IV} centers were first electrooxidized to Ru^V centers, which further oxidize the HMF substrate during electrocatalysis. The presence of the Ru^{III} species[48,49] in the XPS spectra should be attributed to the two-electron reduction of Ru^V centers by the HMF substrate (Fig. 8c).[50] Therefore, the percentage of the Ru^{III} species can indirectly reflect the proportion of the Ru^V active species *in situ* electrogenerated during electrocatalysis. The electronic properties of the Ru species after electrocatalysis differ considerably at the different applied voltages and pH values (Fig. S12†). It is shown that the peak area of the Ru^{III} species gradually increases with the increasing applied anodic potential (Fig. 8c, S12a and b†), strongly illustrating the enhanced oxidation of Ru^{IV} to the Ru^V species, which is also consistent with the results of FTAC voltammetry (Fig. 7a). While maintaining a constant applied anodic potential, the higher pH value of the electrolyte solution also results in a larger peak area of the Ru^{III} species (Fig. S12c and d†), also in good agreement with the FTAC voltammetry results (Fig. 7b and c).

To intuitively explore the influences of the Ru^V species on the eletrocatalytic activities, the proportion of the Ru^{III} species determined by the XPS results is thus plotted against the yield of furanic products (entries 1–5, Table 1). As Fig. 8d shows, the yields of furanic products are positively related to the percentage of the Ru^{III} species, indirectly implying that the electrocatalytic activities also show positive correlation to the proportion of the Ru^V species. Moreover, the yield of DFF is linear to the proportion of the Ru^{III} species, which provides solid proof that Ru^V centers can effectively oxidize HMF to DFF

via a two-electron transfer process with itself being reduced to Ru^{III}, whereas the four-electron transfer process (HMF to FFCA) was limited. When TEMPO was added in the electrocatalytic system, the FFCA yield of 52.4% (entry 6, Table 1) is improved 3.6 times that of the system without TEMPO (entry 2, Table 1); such increased FFCA yield should be attributed to the efficient two-electron oxidation of DFF to FFCA by Ru^V centers given the fact that TEMPO can promote the oxidation of HMF to DFF (Fig. S13†).

Therefore, based on all above analyses and experimental results (CV, FTAC, and XPS data), it can be concluded that Ru^V active species *in situ* generated in the **Ru₄**/PEI-rGO electrocatalyst are responsible for the efficient electrocatalytic oxidation of HMF, and the three-electron oxidized **Ru₄ 1**(3) species performed the best during the electrolysis process. Therefore, the electrocatalytic oxidation mechanism of HMF is proposed as follows; upon electrolysis, in the anodic chamber, the Ru^{IV} centers in the **Ru₄**/PEI-rGO composite was first oxidized to the three-electron oxidation state **1**(3) that can catalyze the conversion of HMF to furanic products with itself being transformed into the Ru^{III} species. In the meantime, the released protons during these processes are further subjected to reduction to hydrogen in the cathodic chamber, accomplishing a complete valorization cycle of HMF to furanic products and hydrogen.

To investigate the stability, long-term bulk electrolysis of **Ru₄**/PEI-rGO was conducted (Fig. 9a and S14†). With prolonging electrolysis, the conversion of HMF gradually increased and reached 71.4% after 12 hours. No obvious changes were observed in the SEM and TEM images (Fig. S15†) of **Ru₄**/PEI-rGO after the long-term reaction compared to that of the fresh **Ru₄**/PEI-rGO composite (Fig. S2†). The FT-IR spectra were further used to determine the possible changes of the composite after long-term electrolysis. As shown in Fig. 9b, the characteristic bands of W=O, W–O–W, and Ru–O–Ru of **Ru₄** POM still remain after 12 hour long-term electrolysis, revealing the intact skeleton structure of **Ru₄**. It is worth mentioning that the slight red shift of characteristic bands could be attributed to the enhanced electronic interaction between **Ru₄** and the PEI-rGO support. In addition, to test the heterogeneity of the **Ru₄**/PEI-rGO electrocatalyst, the amount of Ru in the post-reaction solution after 12 hour electrolysis was quantified to be 0.04 ppm by the ICP test, indicating the stable electrostatic immobilization of **Ru₄** POM onto the PEI-rGO surface. These
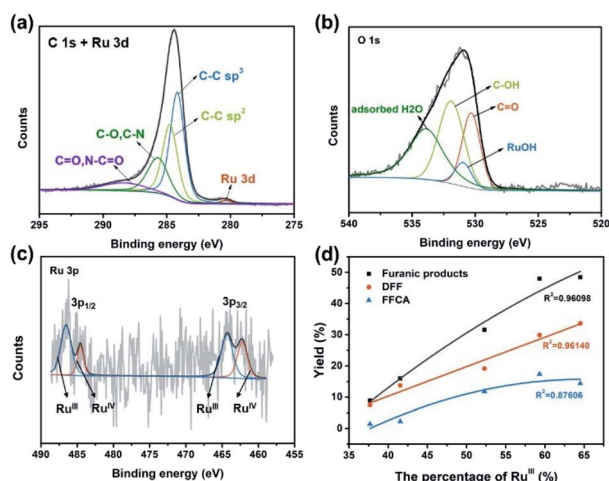
Fig. 8 The high resolution (a) C 1s + Ru 3d, (b) O 1s and (c) Ru 3p XPS spectra of **Ru₄**/PEI-rGO upon electrolysis for 6 h at 0.94 V at pH = 6. (d) The plots of the yields of furanic products *versus* the percentage of the Ru^{III} species.
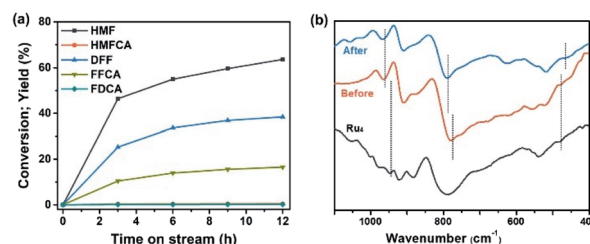
Fig. 9 (a) The long-term bulk electrolysis of **Ru₄**/PEI-rGO at an applied voltage of 0.94 V in pH 6 electrolyte solution. (b) FT-IR spectra of **Ru₄** and **Ru₄**/PEI-rGO before and after long-term electrolysis.

results strongly confirmed that **Ru₄** POM possessed good stability during the electrolysis process in the near-neutral electrolyte.

Conclusions

In conclusion, we have reported the preparation of a **Ru₄**/PEI-rGO electrocatalyst through electrostatic integration of negatively-charged **Ru₄** POM and positively-charged PEI modified rGO. The resulting **Ru₄**/PEI-rGO electrocatalyst can effectively catalyze the oxidation of HMF into value-added furanic products simultaneously coupled with hydrogen production. We have further optimized the reaction parameters during the preparation of catalysts and the electrocatalytic process, including the amount of PEI, the content of **Ru₄** POM, the loading quantity of the composite electrocatalyst onto carbon cloth, the reaction atmosphere, *etc.* Moreover, the influences of a commonly-used additive, TEMPO, on the electrocatalytic activity were also investigated, which not only significantly promoted the electrooxidation of HMF but also regulated the product distribution. Electrochemical techniques (CV, LSV and FTAC) and XPS analyses were employed to disclose the catalytically active species and further get insight into the electrocatalytic oxidation mechanism of HMF as follows; upon electrolysis, in the anodic chamber, the Ru^{IV} centers in the **Ru₄**/PEI-rGO composite was first oxidized to the three-electron oxidation state **1**(3) that can catalyze the conversion of HMF to furanic products with itself being transformed into the Ru^{III} species. In the meantime, the released protons during these processes are further subjected to reduction to hydrogen in the cathodic chamber, accomplishing a complete valorization cycle of HMF to furanic products and hydrogen.

Experimental

Materials and methods

All starting chemicals and solvents for synthesis, characterization, and electrochemical tests were purchased from commercial sources without further purification unless otherwise noted. Rb$_8$K$_2$[Ru$_4$(μ-O)$_4$(μ-OH)$_2$(H$_2$O)$_4$(γ-SiW$_{10}$O$_{36}$)$_2$]·25H$_2$O (**Ru₄**) was synthesized according to a method reported in the literature. TG analysis was performed by using a Mettler Toledo TGA/DSC 1100 thermal analyzer with a rate of 10 °C min^{-1} in an air atmosphere. FT-IR was performed on a Bruker Tensor II with KBr pellets. Scanning electron microscopy (SEM) images and EDX element analysis images were collected on a ZEISS Supra55. HRTEM, HAADF-STEM analysis and element mapping analysis images were collected with an FEI Talos F200X. The zeta potential was obtained by using a NICOMP Z3000 NANO ZLS. The XPS data were collected by using a PHI QUANTERA-II SXM (ULVAC-PHI, Japan) with Al Kα. Inductively coupled plasma optical emission spectrometry (ICP-OES) data were obtained with an Agilent ICPOES730.

Synthetic procedures

Synthesis of Ru₄ POM. Ru₄ POM was synthesized according to a method reported in the literature.[51] K$_8$[γ-SiW$_{10}$O$_{36}$]·12H$_2$O (4.00 g) was first dissolved in 65 mL of H$_2$O, followed by the addition of RuCl$_3$·H$_2$O powder (0.60 g). The solution immediately turned brown, and pH dropped to about 2.6, which was further adjusted to 1.6 by the dropwise addition of HCl solution (6 M). After continuous stirring for 5 min, RbCl solution (2 M) was added dropwise into the mixture. Upon filtration at room temperature, brown plate crystals began to form after 24 h.

Synthesis of GO. GO was prepared by the modified Hummers' method.[52] Graphite powder (1 g) and sodium nitrate (0.5 g) were added into concentrated sulfuric acid (23 mL) and magnetically stirred at 5 °C for 2 h. Potassium permanganate (3 g) was slowly added into the mixture, followed by further stirring at 35 °C for 2 h and 98 °C for 0.5 h. Afterwards, an appropriate amount of hydrogen peroxide was added to react with excess permanganate ions. Finally, brownish graphite oxide was obtained after filtering, washing and freeze-drying.

Synthesis of PEI modified reduced GO (PEI-rGO). GO (80 mg) was dispersed into 20 mL of deionized water and ultrasonicated for 10 min to form a brown homogeneous aqueous solution. 20 mL of PEI aqueous solution (4 mg mL^{-1}) was added dropwise into the GO aqueous solution under stirring and then stirred for 24 h. Upon centrifugation and washing, the precipitate was redispersed into 40 mL of deionized water to further immobilize **Ru₄**. The preparation of PEI-rGO modified with different amounts of PEI is similar to the procedures described above apart from the concentration of PEI aqueous solution of 0, 10, and 50 mg mL^{-1}.

Synthesis of Ru₄/PEI-rGO. The electrocatalyst **Ru₄**/PEI-rGO was prepared as follows; 40 mL **Ru₄** aqueous solution (1 mg mL^{-1}) was added dropwise into 40 mL of PEI-rGO solution under vigorous stirring. After stirring for 24 h, the mixture was transferred into a 100 mL Teflon-lined autoclave and hydrothermally treated at 180 °C for 10 h. Finally, a black solid was collected by centrifugation, washing repeatedly with deionized water and alcohol, and vacuum drying. The preparation of **Ru₄**/PEI-rGO electrocatalysts with different amounts of **Ru₄** is similar to the aforesaid procedures, except for the **Ru₄** aqueous solutions of 0.5, 0.75, and 1.25 mg mL^{-1}.

Electrochemical measurements

Electrochemical measurements were carried out with a CHI 660E potentiostat at room temperature, using an airtight H-type electrochemical cell with the carbon cloth as the working electrode, the Pt sheet as the counter electrode, and a Ag/AgCl electrode as the reference electrode. The working electrode was prepared as the following procedure; catalyst ink was first prepared by sonicating a mixture of 5 mg **Ru₄**/PEI-rGO catalyst and 1 mL Nafion ethanol solution (0.25 wt%) for 30 min. Next, the clean and pre-treated carbon cloth (1 × 1 cm²) was evenly coated with 100 μL catalyst ink, followed by drying under an infrared lamp. LSV and CV measurements were conducted in sequence for the electrocatalysts. 0.5 M HAc/NaAc buffer solution containing 5 mM HMF was used as the electrolyte solution.

This journal is © The Royal Society of Chemistry 2022

J. Mater. Chem. A, 2022, **10**, 19963–19971 | **19969**

EIS measurements were performed in 5 mM HMF at 0.94 V $vs.$ Ag/AgCl. Before testing, the cathodic chamber was purged with CH_4/Ar (20%, volume ratio) gas until no air is detected on a gas chromatography (GC) system, where CH_4 was used as an internal standard. Under the applied voltage, HMF was gradually oxidized at the anode chamber, where the liquid products were analysed on a HPLC system equipped with a Shim-pack GIST C18 column (5 µM, 4.6 × 250 mm) and a UV detector. Methanol and ammonium acetate aqueous solution (5 mM) with a volume ratio of 30 : 70 were used as the mobile phase with a flow rate of 0.3 mL min^{-1}. The detection wavelength is 270 nm. The hydrogen evolution in the cathode chamber was determined on a GC system equipped with a 5A molecular sieve packed column (60/80 mesh, 2 m × 3 mm) and a TCD detector.

FTAC voltammetric measurements were performed with a home-built apparatus, using an applied sine wave perturbation (amplitude 20 mV and frequency 10 Hz) superimposed onto the dc ramp.

HMF conversion, DFF/HMFCA/FFCA/FDCA selectivity, carbon balance and Faraday efficiency (FE) were calculated according to eqn (1)–(4).

$$\text{Con.}_{\text{HMF}} \ (\%) = \left(1 - \frac{\text{moles of HMF in the products}}{\text{initial moles of HMF}} \right) \times 100\% \tag{1}$$

$$\text{Sel.}_{\text{X}} \ (\%) = \frac{\text{moles of X in products}}{\text{the converted moles of HMF}} \times 100\% \tag{2}$$
$$(X = \text{DFF/HMFCA/FFCA/FDCA})$$

$$\text{Carbon balance} \ (\%) = \frac{\sum(\text{moles of C in products})}{\text{moles of C in the converted HMF}} \times 100\% \tag{3}$$

$$\text{FE} \ (\%) = \frac{\text{mole of product formed}}{\text{total charge passed}/(n \times F)} \times 100\% \tag{4}$$

where n is the number of electrons transferred for each product formation, and F is the Faraday constant (96 485 C mol^{-1}).

Author contributions

Hui Zhou: methodology, data curation, formal analysis, investigation, and writing – original draft preparation. Xing Xin and Manzhou Chi: discussions. Tinglu Song: XPS measurement. Yuanyuan Dong and Hongjin Lv: funding acquisition, project administration, conceptualization, supervision, validation, and writing – reviewing and editing.

Conflicts of interest

There are no conflicts to declare.

Acknowledgements

References

1 M. Zhang, Y. Liu, B. Liu, Z. Chen, H. Xu and K. Yan, ACS $Catal.$, 2020, **10**, 5179–5189.

2 W. Liu, W. You, Y. Gong and Y. Deng, $Energy$ $Environ.$ $Sci.$, 2020, **13**, 917–927.

3 W. Liu, Y. Cui, X. Du, Z. Zhang, Z. Chao and Y. Deng, $Energy$ $Environ.$ $Sci.$, 2016, **9**, 467–472.

4 H. Zhao, D. Lu, J. Wang, W. Tu, D. Wu, S. W. Koh, P. Gao, Z. J. Xu, S. Deng, Y. Zhou, B. You and H. Li, $Nat.$ $Commun.$, 2021, **12**, 2008.

5 J. Iglesias, I. Martínez-Salazar, P. Maireles-Torres, D. Martin Alonso, R. Mariscal and M. López Granados, $Chem.$ $Soc.$ $Rev.$, 2020, **49**, 5704–5771.

6 B. You, N. Jiang, X. Liu and Y. Sun, $Angew.$ $Chem.,$ $Int.$ $Ed.$, 2016, **55**, 9913–9917.

7 X. Deng, G.-Y. Xu, Y.-J. Zhang, L. Wang, J. Zhang, J.-F. Li, X.-Z. Fu and J.-L. Luo, $Angew.$ $Chem.,$ $Int.$ $Ed.$, 2021, **60**, 20535–20542.

8 R. Latsuzbaia, R. Bisselink, A. Anastasopol, H. van der Meer, R. van Heck, M. S. Yagüe, M. Zijlstra, M. Roelands, M. Crockatt, E. Goetheer and E. Giling, $J.$ $Appl.$ $Electrochem.$, 2018, **48**, 611–626.

9 M. Park, M. Gu and B.-S. Kim, ACS $Nano$, 2020, **14**, 6812–6822.

10 S. Kar, Q.-Q. Zhou, Y. Ben-David and D. Milstein, $J.$ $Am.$ $Chem.$ $Soc.$, 2022, **144**, 1288–1295.

11 G. Grabowski, J. Lewkowski and R. Skowroński, $Electrochim.$ $Acta$, 1991, **36**, 1995.

12 A. R. Poerwoprajitno, L. Gloag, J. Watt, S. Cychy, S. Cheong, P. V. Kumar, T. M. Benedetti, C. Deng, K.-H. Wu, C. E. Marjo, D. L. Huber, M. Muhler, J. J. Gooding, W. Schuhmann, D.-W. Wang and R. D. Tilley, $Angew.$ $Chem.,$ $Int.$ $Ed.$, 2020, **59**, 15487–15491.

13 S. Barwe, J. Weidner, S. Cychy, D. M. Morales, S. Dieckhöfer, D. Hiltrop, J. Masa, M. Muhler and W. Schuhmann, $Angew.$ $Chem.,$ $Int.$ $Ed.$, 2018, **57**, 11460–11464.

14 L. Gao, Y. Bao, S. Gan, Z. Sun, Z. Song, D. Han, F. Li and L. Niu, $ChemSusChem$, 2018, **11**, 2547–2553.

15 H. Chen, J. Wang, Y. Yao, Z. Zhang, Z. Yang, J. Li, K. Chen, X. Lu, P. Ouyang and J. Fu, $ChemElectroChem$, 2019, **6**, 5797–5801.

16 H. G. Cha and K.-S. Choi, $Nat.$ $Chem.$, 2015, **7**, 328–333.

17 Q. Qin, T. Heil, J. Schmidt, M. Schmallegger, G. Gescheidt, M. Antonietti and M. Oschatz, ACS $Appl.$ $Energy$ $Mater.$, 2019, **2**, 8359–8365.

18 A. Corma, S. Iborra and A. Velty, $Chem.$ $Rev.$, 2007, **107**, 2411–2502.

19 T. Cao, M. Wu, V. V. Ordomsky, X. Xin, H. Wang, P. Métivier and M. Pera-Titus, $ChemSusChem$, 2017, **10**, 4851–4854.

20 N. Li, J. Liu, B.-X. Dong and Y.-Q. Lan, $Angew.$ $Chem.,$ $Int.$ $Ed.$, 2020, **59**, 20779–20793.

21 D. Shi, R. Zheng, C.-S. Liu, D.-M. Chen, J. Zhao and M. Du, *Inorg. Chem.*, 2019, **58**, 7229–7235.

22 S.-B. Yu, Q. Qi, B. Yang, H. Wang, D.-W. Zhang, Y. Liu and Z.-T. Li, *Small*, 2018, **14**, 1801037.

23 H. Lv, W. Guo, K. Wu, Z. Chen, J. Bacsa, D. G. Musaev, Y. V. Geletii, S. M. Lauinger, T. Lian and C. L. Hill, *J. Am. Chem. Soc.*, 2014, **136**, 14015–14018.

24 J. Zhang, M. Zhang, Y. Dong, C. Bai, Y. Feng, L. Jiao and H. Lv, *Nano Res.*, 2022, **15**, 1347–1354.

25 Q. Yin, J. M. Tan, C. Besson, Y. V. Geletii, D. G. Musaev, A. E. Kuznetsov, Z. Luo, K. I. Hardcastle and C. L. Hill, *Science*, 2010, **328**, 342–345.

26 B. Chakraborty, G. Gan-Or, Y. Duan, M. Raula and I. A. Weinstock, *Angew. Chem., Int. Ed.*, 2019, **58**, 6584–6589.

27 Y. Choi, D. Jeon, Y. Choi, J. Ryu and B.-S. Kim, *ACS Appl. Mater. Interfaces*, 2018, **10**, 13434–13441.

28 S.-L. Xie, J. Liu, L.-Z. Dong, S.-L. Li, Y.-Q. Lan and Z.-M. Su, *Chem. Sci.*, 2019, **10**, 185–190.

29 E. Haviv, L. J. W. Shimon and R. Neumann, *Chem.–Eur. J.*, 2017, **23**, 92–95.

30 S.-X. Guo, F. Li, L. Chen, D. R. MacFarlane and J. Zhang, *ACS Appl. Mater. Interfaces*, 2018, **10**, 12690–12697.

31 L. Ni, H. Li, H. Xu, C. Shen, R. Liu, J. Xie, F. Zhang, C. Chen, H. Zhao, T. Zuo and G. Diao, *ACS Appl. Mater. Interfaces*, 2019, **11**, 38708–38718.

32 T. Zhang, A. Solé-Daura, H. Fouilloux, J. M. Poblet, A. Proust, J. J. Carbó and G. Guillemot, *ChemCatChem*, 2021, **13**, 1220–1229.

33 M. Zhao, X.-W. Zhang and C.-D. Wu, *ACS Catal.*, 2017, **7**, 6573–6580.

34 X.-L. Hao, Y.-Y. Ma, H.-Y. Zang, Y.-H. Wang, Y.-G. Li and E.-B. Wang, *Chem.–Eur. J.*, 2015, **21**, 3778–3784.

35 G. Chen, Y. Zhou, Z. Long, X. Wang, J. Li and J. Wang, *ACS Appl. Mater. Interfaces*, 2014, **6**, 4438–4446.

36 E. Nikbakht, B. Yadollahi and M. R. Farsani, *Inorg. Chem. Commun.*, 2015, **55**, 135–138.

37 Z. Li, J. Zhang, X. Jing, J. Dong, H. Liu, H. Lv, Y. Chi and C. Hu, *J. Mater. Chem. A*, 2021, **9**, 6152–6159.

38 J. Lu, Y. Li, S. Li and S. P. Jiang, *Sci. Rep.*, 2016, **6**, 21530.

39 W. Tong, Y. Zhang, Q. Zhang, X. Luan, Y. Duan, S. Pan, F. Lv and Q. An, *Carbon*, 2015, **94**, 590–598.

40 R. Wang, L. Wu, D. Zhuo, Z. Wang and T. Y. Tsai, *Nanoscale Res. Lett.*, 2018, **13**, 351.

41 P. Gobbo, L. Tian, B. V. V. S. Pavan Kumar, S. Turvey, M. Cattelan, A. J. Patil, M. Carraro, M. Bonchio and S. Mann, *Nat. Commun.*, 2020, **11**, 41.

42 A. Sartorel, M. Carraro, G. Scorrano, R. D. Zorzi, S. Geremia, N. D. McDaniel, S. Bernhard and M. Bonchio, *J. Am. Chem. Soc.*, 2008, **130**, 5006–5007.

43 Y. Liu, S.-F. Zhao, S.-X. Guo, A. M. Bond, J. Zhang, G. Zhu, C. L. Hill and Y. V. Geletii, *J. Am. Chem. Soc.*, 2016, **138**, 2617–2628.

44 H. Lv, Z. Li, M. Zhang and X. Xin, *ChemCatChem*, 2021, **13**, 1389–1395.

45 M. Zhang, C. Chen, W. Ma and J. Zhao, *Angew. Chem., Int. Ed.*, 2008, **47**, 9730–9733.

46 C.-Y. Lee, S.-X. Guo, A. F. Murphy, T. McCormac, J. Zhang, A. M. Bond, G. Zhu, C. L. Hill and Y. V. Geletii, *Inorg. Chem.*, 2012, **51**, 11521–11532.

47 Y. Liu, S.-X. Guo, A. M. Bond, J. Zhang, Y. V. Geletii and C. L. Hill, *Inorg. Chem.*, 2013, **52**, 11986–11996.

48 D. J. Morgan, *Surf. Interface Anal.*, 2015, **47**, 1072–1079.

49 W. Wang, S. Guo, I. Lee, K. Ahmed, J. Zhong, Z. Favors, F. Zaera, M. Ozkan and C. S. Ozkan, *Sci. Rep.*, 2014, **4**, 4452.

50 R. Ge, Y. Wang, Z. Li, M. Xu, S.-M. Xu, H. Zhou, K. Ji, F. Chen, J. Zhou and H. Duan, *Angew. Chem., Int. Ed.*, 2022, **61**, e202200211.

51 Y. V. Geletii, B. Botar, P. Kögerler, D. A. Hillesheim, D. G. Musaev and C. L. Hill, *Angew. Chem., Int. Ed.*, 2008, **47**, 3896–3899.

52 Y. Dong, Y. Deng, J. Zeng, H. Song and S. Liao, *J. Mater. Chem. A*, 2017, **5**, 5829–5837.

This journal is © The Royal Society of Chemistry 2022

J. Mater. Chem. A, 2022, **10**, 19963–19971 | **19971**